



A Wigner Potential Decomposition in the Signed-Particle Monte Carlo Approach

Majid Benam^(✉), Mihail Nedjalkov, and Siegfried Selberherr

Institute for Microelectronics, TU Wien, Vienna, Austria
`benam@iue.tuwien.ac.at`

Abstract. The description of the electron evolution, provided by the Wigner equation, involves a force-less Liouville operator, which is associated with particles moving over Newtonian trajectories, and a Wigner potential operator associated with generation of positive and negative particles. These concepts can be combined to develop stochastic algorithms for solving the Wigner equation, consolidated by the so-called signed particle approach. We investigate the option to split the Wigner potential into two parts and to approximate one of them by a classical force term. The purpose is two-fold: First, we search for ways to simplify the numerical complexity involved in the simulation of the Wigner equation. Second, such a term offers a way to a self-consistent coupling of the Wigner and the Poisson equations. The particles in the signed-particle approach experience a force through the classical component of the potential. A cellular automaton algorithm is used to update the discrete momentum of the accelerated particles, which is then utilized along with the Wigner-based generation/annihilation processes. The effect of the approximation on generic physical quantities such as current and density are investigated for different cut-off wavenumbers (wavelengths), and the results are promising for a self-consistent solution of the Wigner and Poisson equations.

Keywords: Wigner function · Potential splitting
Signed-particle approach

1 Introduction

The Wigner function is defined with the Fourier transform of the density matrix expressed in the mean and difference of coordinates in two dimensions:

$$f_w(\mathbf{r}, \mathbf{k}, t) = \frac{1}{(2\pi)^2} \int_{-\infty}^{+\infty} d\mathbf{s} e^{-i\mathbf{k} \cdot \mathbf{s}} \rho\left(\mathbf{r} + \frac{\mathbf{s}}{2}, \mathbf{r} - \frac{\mathbf{s}}{2}, t\right).$$

Furthermore, the finite dimensions of the simulation domain allow the Wigner function to be calculated over finite dimensions and discretized \mathbf{k} values. The physical domain in the simulations analyzed in this paper is a two-dimensional

area of size $(L_x, L_y) = (20 \text{ nm}, 30 \text{ nm})$. We choose the center of the domain to be the origin, and therefore, the position and momentum vectors are discretized as:

$$\begin{aligned} \mathbf{r} &\equiv (x\Delta r, y\Delta r) & -\frac{M}{2} \leq x < \frac{M}{2}, -\frac{N}{2} \leq y < \frac{N}{2} \\ \mathbf{s} &\equiv (m\Delta s, n\Delta s) \\ \mathbf{L} &= (L_x, L_y) \equiv (M\Delta s, N\Delta s) \\ \mathbf{q}\Delta\mathbf{k} &= (p, q) \cdot \left(\frac{\pi}{L_x}, \frac{\pi}{L_y}\right) \equiv \left(p\frac{\pi}{M\Delta s}, q\frac{\pi}{N\Delta s}\right) & -\frac{M}{2} \leq q < \frac{M}{2}, -\frac{N}{2} \leq p < \frac{N}{2} \\ \mathbf{q}'\Delta\mathbf{k} &= (p', q') \cdot \left(\frac{\pi}{L_x}, \frac{\pi}{L_y}\right) \equiv \left(p'\frac{\pi}{M\Delta s}, q'\frac{\pi}{N\Delta s}\right). \end{aligned}$$

Δr and Δs represent the spatial spacing between nodes and are assumed to be equal. \mathbf{s} and \mathbf{q}' are used for performing summations over position and momentum variables. We use the short notation:

$$f(x, y, p, q) \equiv f(x\Delta r, y\Delta r, p\frac{\pi}{M\Delta s}, q\frac{\pi}{N\Delta s}).$$

The Wigner equation, which follows from the von Neumann equation for the density matrix [6], is written in the semi-discrete form as:

$$\left(\frac{\partial}{\partial t} + \frac{\hbar\mathbf{q}\Delta\mathbf{k}}{m^*}\nabla_{\mathbf{r}}\right) f_w(\mathbf{r}, \mathbf{q}, t) = \sum_{\mathbf{q}} V_W(\mathbf{r}, \mathbf{q} - \mathbf{q}') f_w(\mathbf{r}, \mathbf{q}', t). \quad (1)$$

The semi-discrete Wigner potential (WP), which is of central importance in the signed-particle approach, is defined as [4]:

$$V_W(\mathbf{r}, \mathbf{q}) \equiv \frac{1}{i\hbar\mathbf{L}} \int_{-\frac{L}{2}}^{\frac{L}{2}} d\mathbf{s} e^{-i\mathbf{q}\Delta\mathbf{k}\cdot\mathbf{s}} [V(\mathbf{r} + \frac{\mathbf{s}}{2}) - V(\mathbf{r} - \frac{\mathbf{s}}{2})]. \quad (2)$$

2 Wigner Potential Decomposition

Here, we focus on a full discretization, and thus use the fully discretized WP which must be computed at each node [1] becomes:

$$\begin{aligned} V_W(x, y, p, q) &= \frac{1}{i\hbar MN} \sum_{m=-\frac{M}{2}}^{\frac{M}{2}-1} \sum_{n=-\frac{N}{2}}^{\frac{N}{2}-1} e^{-i(pm\frac{\pi}{M} + qn\frac{\pi}{N})} \\ &\quad \times \left[V\left(x + \frac{m}{2}, y + \frac{n}{2}\right) - V\left(x - \frac{m}{2}, y - \frac{n}{2}\right) \right]. \quad (3) \end{aligned}$$

The two-dimensional discrete Fourier transform of a potential $V(x, y)$ in a region of size $M \times N$ is a function $\hat{V}(p, q)$. The pair is given by the equations [5]:

$$\hat{V}(p, q) = \sum_{x=-\frac{M}{2}}^{\frac{M}{2}-1} \sum_{y=-\frac{N}{2}}^{\frac{N}{2}-1} V(x, y) e^{-i2\pi(\frac{px}{M} + \frac{qy}{N})},$$

$$V(x, y) = \frac{1}{MN} \sum_{p=-\frac{M}{2}}^{\frac{M}{2}-1} \sum_{q=-\frac{N}{2}}^{\frac{N}{2}-1} \hat{V}(p, q) e^{i2\pi(\frac{px}{M} + \frac{qy}{N})}.$$

$\hat{V}(p, q)$ can be expressed in polar form, $\hat{V}(p, q) = A(p, q)e^{i\phi(q, p)}$. Since the two-dimensional discrete Fourier transform pair is periodic (k and l being integers),

$$\hat{V}(p, q) = \hat{V}(p + kM, q + lN), \quad V(x, y) = V(x + kM, y + lN),$$

we also assume the physical potential $V(x, y)$ to be periodic so that a shift equal to a multiple of the physical region lengths in the corresponding argument of the potential does not change the value of the potential. It holds:

$$\begin{aligned} & \sum_{m=-\frac{M}{2}}^{\frac{M}{2}-1} \sum_{n=-\frac{N}{2}}^{\frac{N}{2}-1} e^{-i(\frac{\pi m p}{M} + \frac{\pi n q}{N})} \left[V\left(x + \frac{m}{2}, y + \frac{n}{2}\right) \right] = e^{i2(\frac{\pi x p}{M} + \frac{\pi y q}{N})} \\ & \times \sum_{m'=x-\frac{M}{4}}^{x+\frac{M}{4}-1} \sum_{n'=y-\frac{N}{4}}^{y+\frac{N}{4}-1} e^{-i2(\frac{\pi m' p}{M} + \frac{\pi n' q}{N})} \left[V(m', n') \right] = e^{i2(\frac{\pi x p}{M} + \frac{\pi y q}{N})} \hat{V}(2p, 2q), \\ & \sum_{m=-\frac{M}{2}}^{\frac{M}{2}} \sum_{n=-\frac{N}{2}}^{\frac{N}{2}} e^{-i(\frac{\pi m p}{M} + \frac{\pi n q}{N})} \left[V\left(x - \frac{m}{2}, y - \frac{n}{2}\right) \right] = e^{-i2(\frac{\pi x p}{M} + \frac{\pi y q}{N})} \\ & \times \sum_{m'=x-\frac{M}{4}}^{x+\frac{M}{4}-1} \sum_{n'=y-\frac{N}{4}}^{y+\frac{N}{4}-1} e^{i2(\frac{\pi m' p}{M} + \frac{\pi n' q}{N})} \left[V(m', n') \right] = [e^{i2(\frac{\pi x p}{M} + \frac{\pi y q}{N})} \hat{V}(2p, 2q)]^*. \end{aligned}$$

We have used the properties of the discrete Fourier transform, namely periodicity and scaling. Thus, the Wigner potential given in Eq. 3 becomes:

$$V_w(x, y, p, q) = \frac{1}{i\hbar MN} \left\{ e^{i2(\frac{\pi x p}{M} + \frac{\pi y q}{N})} \hat{V}(2p, 2q) - [e^{i2(\frac{\pi x p}{M} + \frac{\pi y q}{N})} \hat{V}(2p, 2q)]^* \right\}. \quad (4)$$

Using Euler's formula, Eq. 4 can be rewritten in a polar form as:

$$V_w(x, y, p, q) = \frac{2}{\hbar MN} A(2p, 2q) \sin[\phi(2p, 2q) + 2\frac{\pi x p}{M} + 2\frac{\pi y q}{N}]. \quad (5)$$

In the following, we show that treating the summation in the right-hand side of Eq. 1 in two separate regions results in the spectral decomposition of the potential profile into a slowly varying classical component and a rapidly varying quantum mechanical component [2]. For each direction we specify a cut-off wavenumber determining the sharpness of the corresponding low-pass filter which is discussed later in more details. The cut-off wavenumber is specified by a cut-off wavelength, $\lambda_{c_x} = \frac{2\pi}{q_{c_x} \Delta k_x}$ and $\lambda_{c_y} = \frac{2\pi}{q_{c_y} \Delta k_y}$. We assume q_{c_x} and q_{c_y} to be

equal and use q_c for both directions. Applying the decomposition, the potential operator on the right-hand side of Eq. 1 can be rewritten as [3]:

$$Qf_w(x, y, p, q) = \sum_{p', q'} V_w(x, y, p', q') f_w(x, y, p - p', q - q') = \sum_{|q'|, |p'| \leq \frac{q_c}{2}} + \sum_{|q'|, |p'| > \frac{q_c}{2}} = Q_{cl} f_w + Q_{qm} f_w$$

Q_{cl} and Q_{qm} represent the classical and potential parts of the potential operator, respectively. We recall that Lagrange's mean value theorem allows to express the increment of a continuous function on an interval through the value of the derivative at an intermediate point of the segment (for small $(m - n)\Delta x$)

$$f(m\Delta x) - f(n\Delta x) \simeq f'(k\Delta x)(m - n)\Delta x \simeq \Delta f(m - n), n \leq k \leq m.$$

Using the notations Δ_p and Δ_q , we calculate the classical potential operator as:

$$\begin{aligned} Q_{cl} f_w(x, y, p, q) &= \sum_{|q'|, |p'| \leq \frac{q_c}{2}} V_w(x, y, p', q') f_w(x, y, p - p', q - q') \\ &\approx \sum_{|q'|, |p'| \leq \frac{q_c}{2}} V_w(x, y, p', q') \left[f_w(x, y, p, q) - \frac{\pi p'}{M} \Delta_p f_w(x, y, p, q) - \frac{\pi q'}{N} \Delta_q f_w(x, y, p, q) \right]. \end{aligned}$$

In the second line, the summation over f_w vanishes as V_w is an odd function in both p and q . Using the polar form of the Wigner potential (Eq. 5), we obtain:

$$\begin{aligned} - \sum_{|q|, |p| \leq \frac{q_c}{2}} \frac{\pi p}{M} V_w(x, y, p, q) &= \frac{-2}{\hbar M N} \sum_{|q|, |p| \leq \frac{q_c}{2}} \frac{\pi p}{M} A(2p, 2q) \sin[\phi(2p, 2q) + 2\frac{\pi x p}{M} + 2\frac{\pi y q}{N}] \\ &= \frac{-1}{\hbar M N} \sum_{|q|, |p| \leq q_c} \frac{\pi p}{M} A(p, q) \sin[\phi(p, q) + \frac{\pi x p}{M} + \frac{\pi y q}{N}] \\ &= \Delta_x \frac{1}{\hbar M N} \sum_{|q|, |p| \leq q_c} A(p, q) \cos[\phi(p, q) + \frac{\pi x p}{M} + \frac{\pi y q}{N}] \\ &= \frac{1}{\hbar} \Delta_x \Re \left\{ \frac{1}{M N} \sum_{|q|, |p| \leq q_c} A(p, q) e^{i\phi(p, q)} e^{i\frac{\pi x p}{M}} e^{i\frac{\pi y q}{N}} \right\} \\ &= \frac{1}{\hbar} \Delta_x \Re \left\{ \frac{1}{M N} \sum_{|q|, |p| \leq q_c} \hat{V}(p, q) e^{i(\frac{\pi x p}{M} + \frac{\pi y q}{N})} \right\} = \frac{1}{\hbar} \Delta_x V_{cl}(x, y). \end{aligned}$$

With a similar approach, we can show that:

$$- \sum_{|q| \leq \frac{q_c}{2}} \sum_{|p| \leq \frac{q_c}{2}} \frac{\pi q}{N} V_w(x, y, p, q) = \frac{1}{\hbar} \Delta_y V_{cl}(x, y).$$

Here, we have introduced the classical potential component:

$$V_{cl}(x, y) = \frac{1}{M N} \sum_{|q|, |p| \leq q_c} \hat{V}(p, q) e^{i(\frac{\pi x p}{M} + \frac{\pi y q}{N})}.$$

This function is real, as can be easily shown by substituting $\hat{V}(p, q)$:

$$\begin{aligned} V_{cl}(x, y) &= \frac{1}{MN} \sum_{|q|, |p| \leq q_c} \sum_{m=-\frac{M}{2}}^{\frac{M}{2}-1} \sum_{n=-\frac{N}{2}}^{\frac{N}{2}-1} V(m, n) e^{i \frac{\pi(x-m)p}{M}} e^{i \frac{\pi(y-n)q}{N}} \\ &= \sum_{m=-\frac{M}{2}}^{\frac{M}{2}-1} \sum_{n=-\frac{N}{2}}^{\frac{N}{2}-1} V(m, n) \cdot \frac{\sin[\frac{\pi q_c(x-m)}{M}]}{\pi(x-m)} \cdot \frac{\sin[\frac{\pi q_c(y-n)}{N}]}{\pi(y-n)}. \end{aligned}$$

In order to calculate V_{cl} , we have a convolution of real functions, the potential $V(x, y)$ and the *sinc* functions in both x and y directions acting as low-pass filters. The convolution involves an infinite summation for an ideal filter. However, we choose our low-pass filter to be bounded to the physical region. V_{cl} at each node in the spatial domain is then calculated as:

$$V_{cl}(x, y) = \sum_{m, n=-\infty}^{+\infty} V_{lp}(x-m, y-n) \cdot V(m, n) \simeq \frac{1}{\Omega(x, y)} \sum_{m=-\frac{M}{2}}^{\frac{M}{2}-1} \sum_{n=-\frac{N}{2}}^{\frac{N}{2}-1} \omega_{xymn} V(m, n).$$

The coefficients ω_{xymn} and $\Omega(x, y)$ are:

$$\omega_{xymn} = \frac{\sin[\frac{\pi q_c(x-m)}{M}]}{\pi(x-m)} \cdot \frac{\sin[\frac{\pi q_c(y-n)}{N}]}{\pi(y-n)}, \quad \Omega(x, y) = \sum_{m=-\frac{M}{2}}^{\frac{M}{2}-1} \sum_{n=-\frac{N}{2}}^{\frac{N}{2}-1} \omega_{xymn}.$$

Therefore, through the introduction of q_c , the input potential $V(x, y)$ is split into a classical and a quantum-mechanical part.

$$V(x, y) = V_{cl}(x, y) + V_{qm}(x, y). \quad (6)$$

$V_{cl}(x, y)$ is the slowly varying part of the potential calculated above by filtering out the high frequency components. $V_{qm}(x, y)$ contains only the high-frequency components and represents the rapidly varying part of $V(x, y)$. It is easily calculated from Eq. 6 after knowing $V_{cl}(x, y)$. Using Eqs. 2 and 3, the fully discretized WP can then be computed at each node using our new approach:

$$V_{qm, W}(x, y, p, q) = \frac{1}{i\hbar MN} \sum_{m=-\frac{M}{2}}^{\frac{M}{2}-1} \sum_{n=-\frac{N}{2}}^{\frac{N}{2}-1} e^{-i(\frac{\pi mp}{M} + \frac{\pi qn}{N})} [V(x + \frac{m}{2}, y + \frac{n}{2}) - V(x - \frac{m}{2}, y - \frac{n}{2})].$$

The Wigner equation in the light of the spectral decomposition will be:

$$\left(\frac{\partial}{\partial t} + \frac{\hbar \mathbf{q} \Delta k}{m^*} \Delta_{\mathbf{r}} - \frac{1}{\hbar} [\Delta_{\mathbf{r}} V_{cl}(\mathbf{r})] \Delta_{\mathbf{q}} \right) f_w(\mathbf{r}, \mathbf{q}, t) = \sum_{\mathbf{q}} V_{qm, W}(\mathbf{r}, \mathbf{q} - \mathbf{q}') f_w(\mathbf{r}, \mathbf{q}', t).$$

As shown in the left-hand side of the modified Wigner equation, V_{cl} gives rise to a local force term which is calculated using the finite difference method. Furthermore, the new Wigner potential ($V_{qm, W}$) on the right-hand side of the equation is calculated from the non-local component of the potential (V_{qm}).

3 Calculating Local Force and Evolving the Particles

The finite difference method suggests to use the two classical potential values from two adjacent nodes to approximate the force:

$$F_x(x, y) = \frac{V_{cl}(x+1, y) - V_{cl}(x-1, y)}{2\Delta r}, \quad F_y(x, y) = \frac{V_{cl}(x, y+1) - V_{cl}(x, y-1)}{2\Delta r}.$$

Here, we focus on the force due to the presence of a dopant in the center; as it is exerted on each particle, the value of the momentum in each direction is updated and lies somewhere between two momentum grid points in the corresponding direction. In the following, a probabilistic approach is discussed and the above-mentioned grid points in the x-direction are named *A* and *B*. When the particles change their momenta, they might jump to points on the momentum grid which are several Δk farther afield. To explain our algorithm, two variables are introduced. The first variable, k_{rnd} , is a random number between 0 and 1. The second one, k_{jump} , is the remaining fractional part of momentum after it is rounded to the smaller point on the momentum grid (*A*), and divided by Δk , therefore, k_{jump} is also always a real number between 0 and 1. Figure 1 illustrates these variables in more details.

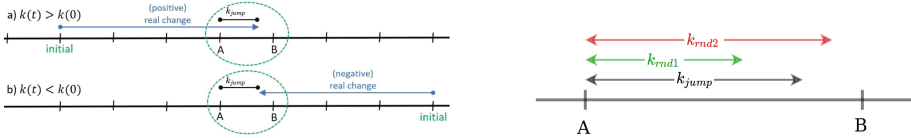


Fig. 1. *Left:* Two possible jumps on the momentum grid. *Right:* A schematic of a possible set of variables (Color figure online)

Without the probabilistic approach, for small momentum changes (compared to Δk), the new momentum is always rounded back to the same point on the momentum grid. In our approach, however, the decision whether to jump to the nearby point on the grid or not is based on a comparison. k_{rnd} is compared to k_{jump} ; if k_{jump} is larger than k_{rnd} (the green case in Fig. 1) the momentum of the particle will jump to the nearby grid point (*B*). Otherwise (the red case in Fig. 1), it remains on the initial grid point *A*. Higher k_{jump} means higher probability of jumping to the nearby grid. The same approach is used in the y-direction.

4 Results

For comparison purposes, we introduced $(\frac{\lambda_c}{\Delta x})$ as a dimensionless input parameter in the ViennaWD simulator [7]. For $\frac{\lambda_c}{\Delta x} = 2$, V_{qm} vanishes as all the possible contributions of the adjacent nodes are canceled out due to the nature of the

sinc function; however, as we increase $\frac{\lambda_c}{\Delta x}$, V_{cl} becomes smoother and V_{qm} gets closer to $V(x, y)$. Potential values at each node in the physical region contribute to V_{cl} (and hence V_{qm}) at all the other nodes through a weighted-average process. The contribution of each node depends on two factors: (1) How far is the node from the target node, (2) How big is q_c (i.e. how small is λ_c). The results for the potential decomposition in the case of a single charge in the center of a $20 \text{ nm} \times 30 \text{ nm}$ region for three different values of λ_c are shown in Fig. 2:

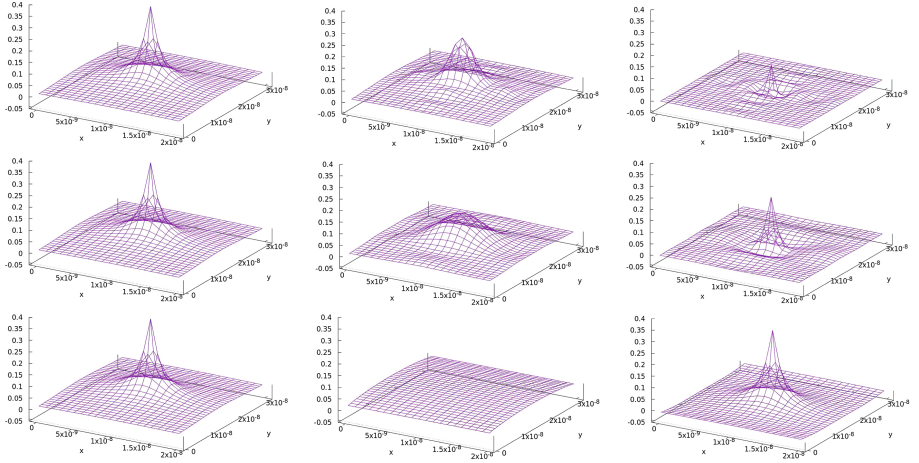


Fig. 2. The potential input (left) and its classical (middle) and quantum (right) components for a single charge in the center of a $20 \text{ nm} \times 30 \text{ nm}$ region for $\frac{\lambda_c}{\Delta x} = 5$ (top row), $\frac{\lambda_c}{\Delta x} = 10$ (middle row), and $\frac{\lambda_c}{\Delta x} = 30$ (bottom row).

Increasing $\frac{\lambda_c}{\Delta x}$ results in a smoother V_{cl} as can be seen in Fig. 2. The right-most graphs show the rapidly varying quantum component of the potential (V_{qm}), which tends to $V(x, y)$ at higher values of λ_c . V_{qm} contains only the rapidly varying part of the potential and dictates the generation rate of particles (γ) at each node. Since the process of particle generation is exponentially related to γ , $N_{t_{n+1}} = N_{t_n} e^{2\gamma(t_{n+1}-t_n)}$, the increase in the number of particles becomes slower which results in fewer annihilation processes and hence improvements in the simulation time. It also reduces the undesirable effects of approximations inherent in the annihilation process [6]. In Fig. 3, the results for different λ_c values and the pure quantum case for $t = 95 \text{ fs}$ are shown. The tendency towards pure quantum behaviour is noticed as we increase λ_c .

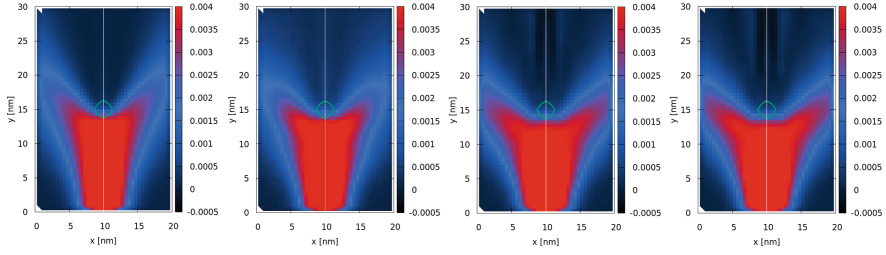


Fig. 3. The density of particles for different values of $\frac{\lambda_c}{\Delta x}$. From left to right: $\frac{\lambda_c}{\Delta x} = 2$ (classical case), $\frac{\lambda_c}{\Delta x} = 10$, $\frac{\lambda_c}{\Delta x} = 30$, and pure quantum (given for reference)

The density values at each point in the physical region are compared to the density values of the pure quantum case by introducing the error ratio:

$$Err_D(x_i, y_j) = \frac{D_{\lambda_c}(x_i, y_j) - D_{qm}(x_i, y_j)}{D_{qm}(x_i, y_j)}.$$

Figure 4 shows the results of the averaged value of this error for different λ_c values. Comparing Figs. 3 and 4, it can be noticed that even for low values of λ_c (high values of q_c), the error remains close to zero for the points in the physical region where the density values are significant. Therefore, we can claim that a spectral decomposition provides a promising step towards coupling the Poisson and Wigner equations. For the regions with lower density values, the improvement in Err_D is evident as we increase λ_c . If quantum effects such as tunneling are to be analyzed, higher values of λ_c are preferred and more reliable.

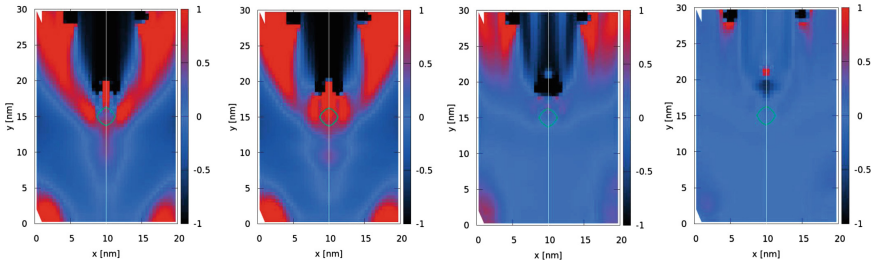


Fig. 4. The error ratio of particle density for different values of $\frac{\lambda_c}{\Delta x}$. From left to right: $\frac{\lambda_c}{\Delta x} = 2$ (classical case), $\frac{\lambda_c}{\Delta x} = 5$, $\frac{\lambda_c}{\Delta x} = 20$, and $\frac{\lambda_c}{\Delta x} = 30$.

As can be seen in Fig. 5, the current values come to a saturated value after around $50fs$, and for different cut-off wavelengths, this saturated value lies within the 10% range of the quantum case.

It is important to note that the accuracy of the decomposition is not linearly related to the value of λ_c as depicted in Fig. 5.

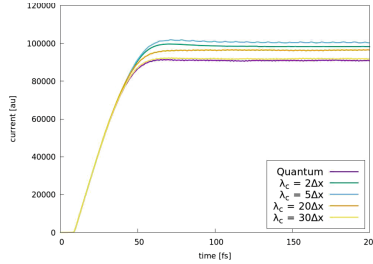


Fig. 5. Current curves for different values of λ_c and the pure quantum case (reference).

5 Discussion and Conclusion

The advantage of utilizing a potential splitting approximation is two-fold. On one hand, the statistics governing the generation of particles are modified so that the ensemble of particles experiences fewer annihilation processes. On the other hand, using this approach, the momentum values are updated according to V_{cl} and the local force term. Particles are accelerated in each time step and the value of the momentum, while remaining on the momentum grid, is no longer constant through the simulation time. Averaged physical quantities such as current and density show a decent similarity to the pure quantum case, especially for $\lambda_c \gg \Delta r$. Coupling the quantum character of carrier transport with the classical evolution of particles seems to be a promising step towards an efficient self-consistent coupling of the Wigner and Poisson equations.

Acknowledgements. This research has been supported by the Austrian Science Fund through the project FWF-P29406-N30.

References

1. Ellinghaus, P.: Two-Dimensional Wigner Monte Carlo Simulation for Time-Resolved Quantum Transport with Scattering. Dissertation, Institute for Microelectronics, TU Wien (2016)
2. Gehring, A., Kosina, H.: Wigner function-based simulation of quantum transport in scaled DG-MOSFETs using a Monte Carlo method. *J. Comput. Electron.* **4**(1–2), 67–70 (2005)
3. Nedjalkov, M., Querlioz, D., Dollfus, P., Kosina, H.: Wigner function approach. In: Vasilevski, D., Goodnick, S. (eds.) *Nano-Electronic Devices: Semiclassical and Quantum Transport Modeling*, pp. 289–358. Springer, New York (2011). https://doi.org/10.1007/978-1-4419-8840-9_5
4. Querlioz, D., Dollfus, P.: *The Wigner Monte Carlo Method for Nanoelectronic Devices. A Particle Description of Quantum Transport and Decoherence*. Wiley, Hoboken (2010)
5. Gonzalez, R.C., Woods, R.E.: *Digital Image Processing*, 3rd edn, pp. 154–155. Prentice Hall, New York (2008)

6. Ellinghaus, P., Nedjalkov, M., Selberherr, S.: Optimized particle regeneration scheme for the Wigner Monte Carlo method. In: Dimov, I., Fidanova, S., Lirkov, I. (eds.) NMA 2014. LNCS, vol. 8962, pp. 27–33. Springer, Cham (2015). https://doi.org/10.1007/978-3-319-15585-2_3
7. ViennaWD - Wigner Ensemble Monte Carlo Simulator. <http://www.iue.tuwien.ac.at/software/viennawd>